Modification of 1D TiO_2 nanowires with GaO_xN_y by atomic layer deposition for TiO_2@GaO_xN_y core-shell nanowires with enhanced photoelectrochemical performance

Jia-Jia Tao[‡,a], Hong-Ping Ma[‡,a], Kai-Ping Yuan[a], Yang Gu[a], Jian-Wei Lian[a], Xiao-Xi Li[a], Wei Huang[a], Michael Nolan[b,*], Hong-Liang Lu[a,*] and David-Wei Zhang[a]

[a] State Key Laboratory of ASIC and System, Shanghai Institute of Intelligent Electronics & Systems, School of Microelectronics, Fudan University, Shanghai 200433, China

[b] Tyndall National Institute, University College Cork, Lee Maltings, Dyke Parade, Cork T12 R5CP, Cork, Ireland

E-mail: Michael.nolan@tyndall.ie (M. Nolan), honglianglu@fudan.edu.cn (H-L Lu);

‡, These authors contributed equally

Abstract

As a well known semiconductor that can catalyse the oxygen evolution reaction, TiO_2 has been extensively investigated for its solar photoelectrochemical water properties. Unmodified TiO_2 shows some issues, particularly with respect to its photoelectrochemical performance. In this paper, we present a strategy for the controlled deposition of controlled amounts of GaO_xN_y cocatalysts on TiO_2 1D nanowires (TiO_2@GaO_xN_y core-shell) using atomic layer deposition. We show that this modification significantly enhances the photoelectrochemical performance compared to pure TiO_2 NW photoanodes. For our most active TiO_2@GaO_xN_y core-shell nanowires with a GaO_xN_y thickness of 20 nm, a photocurrent density up to 1.10 mA cm^{-2} (at 1.23 V *vs* RHE) under AM 1.5 G irradiation (100 mW cm^{-2}) has been achieved, which is 14 times higher than that of unmodified TiO_2 NWs. Furthermore, the band gap matching with TiO_2 enhances absorption of visible light over unmodified TiO_2 and the facile oxygen vacancy formation after deposition of GaO_xN_y also provides active sites for water activation. Density functional theory studies of model systems of GaO_xN_y-modified TiO_2 confirm the band gap reduction, high reducibility and ability to activate

water. The highly efficient and stable systems of TiO_2@GaO_xN_y core-shell nanowires with ALD deposited GaO_xN_y demonstrates a good strategy for fabrication of core-shell structures that enhances the photoelectrochemical performance of readily available photoanodes.

Keywords: TiO_2@GaO_xN_y nanowires; Core-shell nanoarchitecture; Photoelectrochemical performance; Atomic layer deposition.

1. Introduction

As a potentially efficient and sustainable strategy for addressing the global energy problem, particularly for the production of hydrogen, the photocatalytically driven splitting of water using semiconductor catalysts has been widely studied and applied in modern society.[1,2] During recent decades, photocatalytic systems based on two or more semiconductors have been constructed to meet the requirements for a high photoelectrochemical (PEC) activity for water splitting.[3,4] In general, in these systems, one semiconductor material can enhance light absorption while the second semiconductor material can provide more reaction sites and catalytic activity. Additionally, the energy level matching between the two semiconductors can drive effective charge separation and transfer of electrons (e^-) and holes (h^+) at the interfaces or junctions.[5] Since Fujishima et al.[6] first studied the PEC performance for electrochemical photocatalysis of water over TiO_2, TiO_2 based materials with different size, structure, morphology, or crystal phase have been widely studied and reported for their environmentally benign nature, stability, and cost-efficiency.[7] In terms of nanostructures, one-dimensional TiO_2 nanoarrays, including nanowires (NWs), nanotubes (NTs) and nanorods (NRs), have proven to be promising photoanode materials due to unique geometric advantages offered by these structures. These nanoarray-based semiconductor materials show large specific surface area and enhanced activity, as well as a direct transport path for charge carriers.[8-10]

Despite their advantages, the practical application of TiO_2 nanoarrays still faces

two primary problems. One is the large band gap which means that TiO_2 can only absorb ultraviolet light, which results in a low utilization rate of sunlight, and low energy conversion. The second problem is that the photogenerated excitons (i.e. e^- and h^+) in the conduction (CB) and valence bands (VB) show high recombination rates for both radiative and non-radiative processes, which greatly reduces the efficiency of PEC water splitting.[11] Heterojunctions or interfacial structures using narrow bandgap semiconductors together with TiO_2 is a well-studied strategy to address these problems.

In recent work, it has been discussed that photocatalysts using cations with d^{10} electronic configurations such as Se^{4+}, Ge^{4+}, In^{3+}, Sb^{5+}, and Ga^{3+} ions[12-14] can realize visible light catalytic reaction. The enhanced performance is suggested to come from high band dispersion of hybridized *sp* orbitals in semiconductors with d^{10} conduction bands, which promotes high electron mobility to enhance the photocatalytic performance.[15] In addition, many researchers focus on the group III nitrides for their excellent optical and unique semiconductor properties. Previously, Bae et al.[16] reported bulk GaN for sustained water splitting due to its chemical stability and suitable CB and VB levels. However, the large band gap of 3.4 eV of phase-pure GaN limits absorption of visible light, and the recombination of photogenerated e^- and h^+ also hinders water oxidation. Alternatively, Hassan et al.[17] fabricated ZnS/GaN photoanodes for enhancing PEC performance, which was ascribed to the type-II band alignment of the heterojunction. Additionally, Ma et al.[18] designed ZnO-GaON core-shell nanowires resulting in high PEC performance which can be tuned by the thickness of the GaON

layer. Interestingly, Patil et al.[19] developed the GaN/ZnO/MWCNTs photoanode, which showed high the PEC performance under visible light irradiation. This improved performance is attributed to the presence of Zn *3d* and N *2p* orbitals in the upper VB, which provides the *p-d* repulsion to shift the VB maximum upwards and reduce the band gap.[20] Similarly, Khan et al.[21] prepared a GaON/ZnO nanoarchitecture with increased hole mobility for PEC performance, which arises from the large dispersion of hybridized O 2p, Zn 3d, and N 2p orbitals.

Hence, taking advantage of the band dispersion in GaO_xN_y, which is driven by the hybridization of O *2p* and N *2p* states with Ga *3d* orbitals in the VB, the top of the VB can be raised and hole mobility enhanced. The unique GaO_xN_y modified nanostructured semiconductors can reduce the suppression of the electron diffusion as well as charge recombination during the PEC process. A conductive electrode composed of GaO_xN_y modified semiconductor material and FTO promoted the charge separation under the applied external electric field.[22] In view of the advantages of GaO_xN_y and TiO_2 NWs described above, we explore if a nanoarchitecture composed of GaO_xN_y nanocluster modifying 1D TiO_2 NWs can exhibit good photoelectrochemical performance such that it may be later used in the oxygen evolution reaction for water splitting.

Reported methods for synthesizing GaO_xN_y include hydrothermal, magnetron sputtering, chemical vapor deposition (CVD).[23-25] Obviously, these methods are not only complex and tedious, but are also unable to achieve accurate control of film thickness and composition of GaO_xN_y. Atomic layer deposition (ALD) which is widely

used in the semiconductor industry shows significant advantages in control of the precise film thickness and deposition for a layer-by-layer growth mechanism.[26] Up to now, the direct growth of GaO_xN_y utilizing ALD has not been studied and reported.

In this paper, we developed a method to synthesize 1D TiO_2@GaO_xN_y core-shell NWs by combining hydrothermal TiO_2 NW synthesis together with ALD for GaO_xN_y deposition on the NWs. This allows for the first time the precise control of the core-shell nanoarchitecture, and the influence of the resulting morphology and optical properties on the PEC performance are also investigated for the first time. The results show that a photocurrent density in TiO_2@20 nm-GaO_xN_y core-shell nanowires (TG20 NWs) up to 1.10 mA cm^{-2} is achieved. The photocurrent density value of TG20 is 14 times larger than that of TiO_2 NWs and the materials show high stability at this current density for 10 hours. In addition, the results of density functional theory (DFT) calculations give insight into the stability of TG NWs systems, the effect of GaO_xN_y deposition on the energy gap of TiO_2 and the enhanced activity towards water dissociation which is important for future work on the water splitting reaction.

2. Experimental Section

Materials and Reagents

Tetrabutyl titanate ($Ti(OBu)_4$, 98%), hydrofluoric acid (HCl, 36-38% by weight), sodium sulfate anhydrous (Na_2SO_4, 98%), ethanol (C_2H_5OH), acetone (CH_3COCH_3), and isopropanol (C_3H_8O), were purchased from Sinopharm Chemical Reagent Co., Ltd. (Shanghai, China). Fluorine-doped tin oxide (FTO)-coated glass substrates (resistance

<14 ohm/sq, transmittance >90%) were purchased from Wuhan Jinge-Solar Energy Technology Co., Ltd. (Wuhan, China). The deionized (DI) water used in the experiments was obtained from local sources. All the chemicals in the experiment were weighted by a METTLER TOLEDO ME 204 balance.

Synthesis of TiO_2 NWs

The TiO_2 NWs were fabricated on FTO substrates (2 cm × 1 cm) by a facile hydrothermal method. Prior to the hydrothermal process, the FTO substrates were successively cleaned in an ultrasonicator with acetone, alcohol, and DI water for 15 min, respectively. Then, they were dried with a N_2 stream and placed in a reaction solution in a Teflon-lined stainless steel autoclave, with the FTO side facing up at 60 ° against the wall. Typically, the reaction solution included 0.25 mL tetrabutyl titanium, 15 mL DI water, and 15 mL hydrofluoric acid. The hydrothermal reaction was maintained at 150 °C. After 4 hours, the as-prepared TiO_2 NWs were washed with ethanol and DI water several times, and then dried for further use.

Synthesis of TiO_2@GaO_xN_y core-shell NWs

The TiO_2@GaO_xN_y core-shell NWs were synthesized by deposition of GaO_xN_y using plasma enhanced atomic layer deposition (PE-ALD, Beneq TFS-200). For deposition of GaO_xN_y, the TiO_2 NWs were placed in the PE-ALD chamber, and trimethyl gallium (TMGa), NH_3, and O_2 were chosen as the typical precursors for GaO_xN_y deposition. The flow ratio of O_2 to NH_3 was 95:5 standard cubic centimeters per minute (sccm). In our PE-ALD process, the deposition temperature is kept at 200 °C

while the plasma power is set at 200 W.

An ALD cycle is composed of four steps: pulse 1 - purge 1 - pulse 2 - purge 2. Accordingly, one ALD cycle for GaO_xN_y is described as follows: TMGa pulse (15 ms) - Ar purge (10 s) - ammonia plasma pulse (15 s) - Ar purge (10 s). A schematic diagram of one ALD cycle of GaO_xN_y deposition is shown in Fig. S1. We note that O_2 and NH_3 are simultaneously introduced into the chamber after the plasma has been turned on. Thus, the mixture of O_2 and NH_3 gas reacts only with surface bound TMGa during the plasma process. By changing the number of ALD cycles, it is possible to prepare a series of TiO_2@GaO_xN_y core-shell NWs with different thicknesses of GaO_xN_y. The number of PE-ALD cycles for GaO_xN_y deposition ranges from 100 to 500 cycles. The thickness of GaO_xN_y was estimated to be 5 (100 cycles), 10 (200 cycles), 15 (300 cycles), 20 (400 cycles), and 25 nm (500 cycles): the samples will be denoted as TG5, TG10, TG15, TG20, and TG25, respectively. The samples are characterized and used in PEC measurements as deposited with no post-deposition annealing. For comparison of substrates, pure GaO_xN_y films of the same thickness were also grown on Si substrates at the same time in order to further study their properties.

Characterization

The crystal structure of the core-shell samples was investigated by XRD (MAC, M18XHF) using Cu Kα radiation. Fourier transform infrared (FTIR) spectroscopy (Nicolet Nexus 470) and Raman spectroscopy (Spex 403 Raman microscope with 532 nm argon ion laser) were used to determine the chemical bonding characteristics of

samples. The thickness and elemental composition of pure GaO_xN_y thin films were measured by spectroscopic ellipsometry (SE, SOPRA, GES-5E) and glow discharge optical emission spectroscopy (GDOES, HIOKI, 200D). The morphology of the samples was exhibited using field-emission scanning electron microscopy (FESEM, Hitachi, S4800), and transmission electron microscope (TEM, Tecnai G^2 S-TWIN). A UV-Vis spectrophotometer (Cary 500, Varian Co.) was employed to characterize the optical properties. Energy dispersive X-ray (EDX) and elemental mapping images were obtained using a JEOL JEM-2100 electron microscope. Photoluminescence (PL) spectra were measured with a fluorescence spectrophotometer (Hitachi F-4500) at an excitation wavelength of 320 nm under ambient conditions. X-ray photoelectron spectroscopy (XPS) measurements were obtained with on a Thermo Scientific ESCA Lab 250 spectrometer that used monochromatic Al Kα as the X-ray source, with a hemispherical analyzer and sample stage with multiaxial adjustability to obtain the elemental chemical states and surface composition. All the binding energies were calibrated by the C 1s peak at 284.6 eV.

Photoelectrochemical Measurements

The photoelectrochemical experiments were carried out on a CHI600D electrochemical workstation (ChenHua Instruments Co. Ltd, China). In this system, the working electrode is the FTO substrates onto which the core-shell nanowires were grown, with dimensions 1 cm × 1 cm. A Pt plate is used as the counter electrode, and an Ag/AgCl electrode is used as the reference electrode. The electrolyte is 0.5 M

Na_2SO_4 aqueous solution (pH = 6.8). A 500 W Xe arc lamp (PLS-SXE 300C, Beijing Perfectlight Co., Ltd.) was used for the irradiation source to simulate sunlight (100 mW cm^{-2}). The electrolyte was stirred and purged with high-purity N_2 for 1 h before each measurement.

From the Nernst equation: E (RHE) = E (Ag/AgCl) + 0.01976 V+ 0.0591*pH, the measured potentials *versus* the Ag/AgCl electrode were converted to the reversible hydrogen electrode (RHE). The scan rate of the linear sweep voltammetry (LSV) curves with light on and off were kept at 20 mV s^{-1}. Time-dependent photocurrent response (*I-t*) curves were obtained with light/dark cycles of 20 s at an applied potential of 1.23 V *vs* RHE. The electrochemical impedance spectroscopy (EIS) plots were measured in the frequency range of 10^{-1} Hz to 10^5 Hz under an ac amplitude of 2 mV. The incident photon to current conversion efficiency (IPCE) was measured by irradiating with monochromatic light. The different wavelength of incident light (in the range of 360-470 nm) were achieved by using a monochromatic filter. The IPCE values are calculated from the following equation:

$$IPCE\ (\%) = (1240I)/(P\lambda) \quad (1)$$

where I is the measured photocurrent density at a specific wavelength, P is the measured irradiance at this wavelength, and λ is the wavelength of the incident light.[27]

Computational Methods

The spin-polarized DFT calculations are carried out with the VASP5.4[28] code

using projector augmented wave (PAW) potentials[29] and the Perdew-Wang (PW91)[30] exchange correlation functional. The plane-wave energy cut-off is 400 eV and Ti is described with 4 valence electrons, Ga with 13 valence electrons, O with 6 valance electrons, N with 5 valance electrons and H with 1 electron potential. The convergence criteria for the energy minimization and force relaxation are 10^{-4} eV and 0.02 eV/Å. The size of the surface supercell is such that k-point sampling is at the Γ-point and aspherical gradient corrections were applied throughout. Gaussian smearing (ISMEAR = 1) and σ = 0.1 eV is used throughout.

A Hubbard +U correction (DFT+U) is used for the Ti *3d* states in which the value of U (Ti 3d) = 4.5 eV, which is consistent with previous work.[31] This correction is necessary to consistently describe the partially filled Ti 3*d*-orbital that is found in reduced Ti^{3+} states, which can be produced by reduction of Ti-oxides.[32] The computed bulk lattice parameters for rutile are $a = b = 4.614$ Å and $c = 2.962$ Å. The model for the rutile TiO_2 (110) surface consists of an 18 atomic layer slab in a (2×4) surface supercell expansion of rutile (110). Periodic images are separated by a vacuum gap of 15 Å. The Ga-oxynitirde modifier is modelled as nanoclusters of composition $Ga_6O_5N_4$ and $Ga_6O_6N_3$ and these are first relaxed in the gas phase as free clusters. We consider each GaO_xN_y nanocluster adsorbed in different configurations at the rutile (110) surface and adsorption energies are computed from:

$$E_{ads} = E_{surf+NC} - E_{surf} - E_{NC} \quad (2)$$

where $E_{surf+NC}$, E_{surf}, and E_{NC} are the total computed energies of the

heterostructured of $TiO_2@GaO_xN_y$, the surface of rutile (110), and the gas-phase nanocluster. The $TiO_2@GaO_xN_y$ heterostructure is relaxed with no constraints on the structure of the nanocluster.

To model reduction of $TiO_2@GaO_xN_y$ we use oxygen vacancy formation in which one oxygen from the GaO_xN_y nanocluster is removed and we computed the vacancy formation energy as follows:

$$E_{vac} = E(GaO_{x-1}N_y\text{-r110}) - E(GaO_{x-1}N_y\text{-r110}) + \frac{1}{2}E(O_2) \qquad (3)$$

Where $E(GaO_{x-1}N_y\text{-r110})$ and $E(GaO_{x-1}N_y\text{-r110})$ are the total energies of the $TiO_2@GaO_xN_y$ heterostructured with and without an oxygen vacancy and the energy is refered to half the total energy of a free gas-phase O_2 molecule computed with the same computational set-up as the surface calculations. Bader charge analysis[33] and computed spin magnetisations are used to investigate oxidation states and localisation of charge. For an unmodified TiO_2 rutile (110) surface the Bader charges for Ti sites are in the range 1.2-1.3 electrons, which is attributed to an oxidation state of Ti^{4+}; O^{2-} sites of the surface have computed Bader charges in the range 7.1-7.2 electrons. Oxygen ions of the cluster and surface are denoted O_C and O_S, respectively, and Nitrogen in the modifier is denoted as N_C.

To investigate the interaction of water at GaO_xN_y-TiO_2 heterostructures, a water molecule is adsorbed in different configurations at the GaO_xN_y modifier. The adsorption energy is computed from:

$$E_{ads} = E_{surf+\mathrm{H_2O}} - E_{surf} - E_{\mathrm{H_2O}} \quad (4)$$

where $E_{surf+\mathrm{H_2O}}$, E_{surf} and $E_{\mathrm{H_2O}}$ denote the energies of the H_2O molecule adsorbed at the GaO_xN_y-TiO_2 structure, GaO_xN_y-TiO_2 and the gas phase H_2O molecule, respectively.

3. Results and discussion

Formation and characterization

Scheme 1 presents an illustration of the TiO_2-GaO_xN_y core-shell NW (denote TG) preparation process *via* our two-step method. 1D TiO_2 NWs were prepared by a hydrothermal reaction, followed by deposition of GaO_xN_y on the TiO_2 NWs by PEALD technology, and formation of TG core-shell NWs. A series of TG core-shell NWs is obtained by varying the number of PE-ALD cycles from 100 to 500 cycles. A schematic diagram of one ALD cycle of GaO_xN_y deposition is shown in Fig. S1.

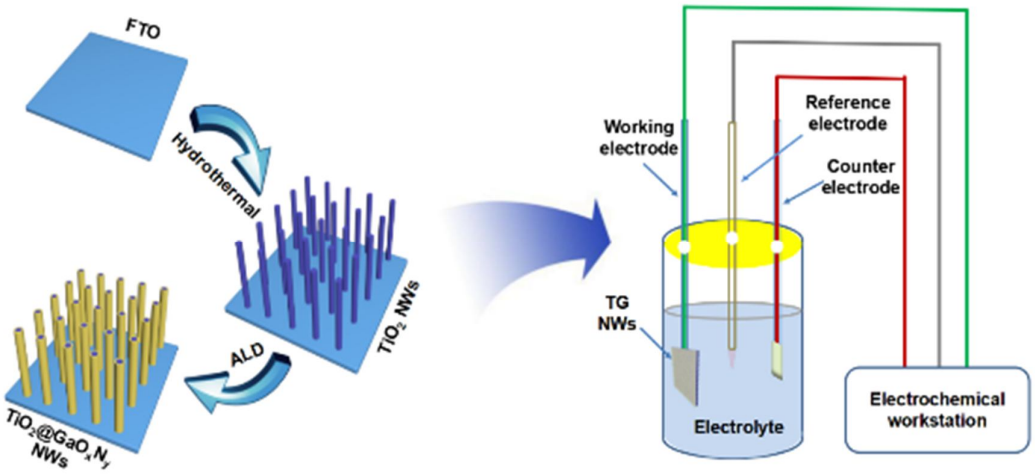

Scheme 1 Fabrication process of TiO_2@GaO_xN_y core-shell NWs, and the PEC testing process.

XRD measurements were used to determine the crystallographic structures of pure TiO_2 and TG NWs and the diffractograms are displayed in Fig. 1(a) for FTO, TiO_2, and a selection of TG nanowires. The XRD pattern for the bare FTO substrate allows for comparison of bare FTO and modified FTO. For the pure TiO_2 NW sample, the three main diffraction peaks centered at 2θ = 36.953°, 63.649°, and 70.721° can be assigned to the (101), (002), and (112) crystal facets of rutile TiO_2[34] PDF # 88 - 1175, with the lattice constants of *a*, *b* =0.452 nm and *c* =0.294 nm. The (002) peak shows a strong and sharp feature, suggesting that the nanowires grew along the (001) direction. No other impurity phase was observed. In the TG NWs, no new peaks corresponding to GaO_xN_y can be observed, while the peaks identified for rutile TiO_2 persist. This is due to the fact that the low content and high dispersion of non-crystalline GaO_xN_y deposited on the surface of the TiO_2 NWs will be amorphous and are too small to be observed with XRD. Interestingly, the (101) peak of rutile disappears at the highest loading of GaO_xN_y, TG25, which indicates that for thinner deposits of GaO_xN_y, the ALD process has only a minor influence on the phase composition and crystallinity of TiO_2 NWs.

Raman spectra were measured to determine the phase structure. As shown in Fig. 1(b), all TG NW samples exhibit the three characteristic rutile Raman vibrational modes at A_{1g} (592 cm^{-1}), E_g (427 cm^{-1}) and E_{2H} (217 cm^{-1}).[35] Although the peak intensity and sharpness of these peaks related to the Raman vibrations of rutile TiO_2 increases as the thickness of GaO_xN_y increases, no Raman peaks characteristic of GaO_xN_y or characteristic of significant structural modifications to the TiO_2 NWs are present, which

is in agreement with XRD results reported above.

FTIR spectra were also recorded to demonstrate the effect of the GaON coating on the IR active vibrational modes of TiO_2 NWs with the different GaO_xN_y thicknesses; these are shown in Fig. 1(c). The FTIR spectrum of the pure TiO_2 NWs is very similar to that of TiO_2 NWs as previously reported.[36] The absorption peaks at 523, 670, and 1162 cm^{-1} are the characteristic vibrations of the Ti-O-Ti networks in TiO_2. After deposition of GaO_xN_y, the vibrational peaks characteristic of GaO_xN_y appeared in TG NWs. The absorption peaks at 778, 877, and 1029 cm^{-1} are related to the typical stretching modes of aromatic Ga-O-N as described in the literature.[21] The data in ref.[21] are for GaON-ZnO, with peaks at 690, 811, 921 and 1025 cm^{-1}. There is good correspondence between the peaks at 1029/1025, 921/877 and 778/811 cm^{-1}, with any differences arising from the different interactions and interface structures between GaON and ZnO/TiO_2. The peak at 669 cm^{-1} is due to Ga-O vibrations of Ga_2O_3.[37] Moreover, the lack of Ti-O-Ti stretching vibrations at 1162 cm^{-1} implies full coverage of GaO_xN_y over TiO_2 NWs. The existence of GaO_xN_y on TiO_2 NWs can be therefore confirmed on the basis of FTIR spectra, which will be further confirmed with depth profiling and microscopy observations discussed below.

To determine the thickness, change in composition with depth, and the distribution and uniformity of Ga, O N and Ti, a typical GaO_xN_y with 200 PE-ALD cycles deposited on a Si substrate was characterized by spectroscopic ellipsometry (SE) and glow discharge optical emission spectroscopy (GDOES). From the SE results, the thickness

of GaO_xN_y after 200 cycles of deposition is 10 nm, the refractive index value (n) is 1.740, and the extinction coefficient (k) is 6.51×10^{-3} at a wavelength of 632.8 nm. The SE data both measured and fitted and optical constants are shown in Fig. S2(a) and (b).

The GDOES depth profiles for a 10nm GaON film are shown in Fig. 1(d). The time needed for complete etching of the GaO_xN_y is 2.5 s. Overall, a homogeneous elemental distribution of Ga, O, and N was detected in the sample. From the GDOES analysis of elements, the highest intensity in GaO_xN_y sample was for the Ga signal, with decreased intensity for the N signal, and the lowest intensity for the O signal. The relatively large amount of N and O in GaO_xN_y film in this work in PEALD grown GaO_xN_y offers advantages when compared to traditional film deposition technologies such as hydrothermal method, CVD, and ALD. Similar phenomena were also investigated during the growth of AlON films in our previous report,[38] which are more conducive for fabrication and applications in the field of electronic devices and catalysts.

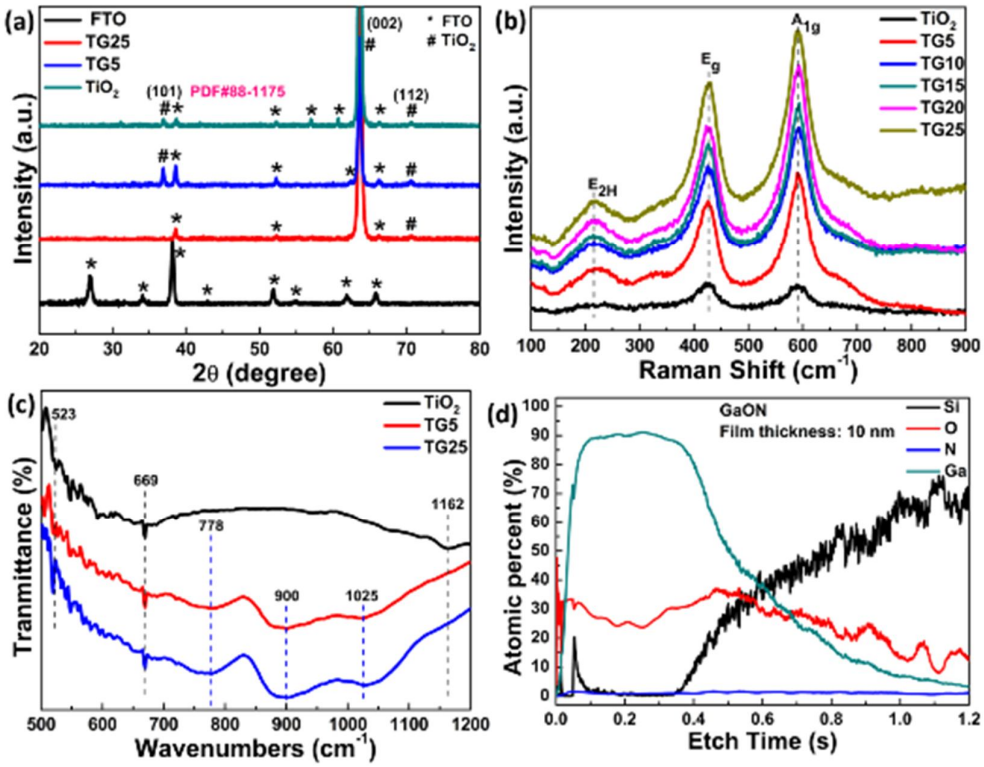

Fig.1 (a) XRD patterns, (b) Raman spectra, and (c) FTIR spectra of pure TiO_2 NWs and TG NWs. (d) The GDOES depth profile is shown for elemental Ga, O, and N elements for representative GaO_xN_y film with thickness of 10 nm deposited on the Si substrate.

SEM images of the FTO glass substrate, pure TiO_2 NWs from hydrothermal synthesis, and a TG10 core-shell nanowires sample are shown in Figure 2(a)-(c). Fig. 2(a) shows that the conductive FTO surface was covered by columnar grains. After hydrothermal NW synthesis, the FTO surface was covered by TiO_2 NWs, which are shown in Fig. 2(b). The TiO_2 NWs are tetragonal with a square facet on the top and the average diameter and length are approximately 20 nm and 1 μm, respectively. Additionally, the top facets of the TiO_2 NWs contain many step edges (the inset of Fig.

2(b)), which are sites for further growth of the NWs. The side facets are smooth, and as a result, growth at the side is disfavored. Therefore, the TiO_2 NWs provide abundant highly accessible interfaces for the PE-ALD process of the GaO_xN_y shell. After the deposition of the GaO_xN_y shell layer from 200 PE-ALD cycles (Fig. 2c), the TG core-shell structure still maintains the TiO_2 NW structure, but the surfaces became more obviously rough along the entire length. Notably, the top of TG core-shell NWs change shape from tetragonal to circular, as shown in the inset of Fig. 2(c). High crystal surface energy and roughness of (001) facet are more favorable for GaO_xN_y deposition and nucleation, as seen in the Fig. 2(b) and (c). In addition, the aspect ratio of (110) facet also provides favorable conditions for uniform deposition of GaO_xN_y, which is consistent with our previous reports[21,39].When we run 100, 200, 300, 400 and 500 cycles PE-ALD cycles, the thicknesses of GaO_xN_y samples measured from SE are 4.97, 9.12, 14.41, 18.49, and 26.71 nm, respectively. The apparent thickness is therefore linear with the number of PE-ALD cycles. On the contrary, compared to ALD technique, the traditional deposition techniques for synthesizing GaO_xN_y include hydrothermal and chemical methods which show some disadvantages in the precise control of morphology and composition of GaO_xN_y. Patil et al. prepared the ternary heterostructure GaN/ZnO/MWCNTs by using metal organic chemical vapour deposition techniques, which cannot precisely control the composition of GaN[19]. Khan et al. fabricated the GaON/ZnO nanoarchitectures with uncontrolled morphologies by the hydrothermal method[21]. Hu et al. reported the synthesis of wurtzite-like GaON photocatalysts by the nitridation of $Ga(OH)_3$ with NH_3 in a temperatures range between

550 and 900 ℃, in which the morphologies and components of GaON film cannot be regulated accordingly[25]. Therefore, we show that by simply varying the number of ALD cycles, the thickness of the GaO_xN_y shell can be precisely tuned, in contrast to these other, less controlled approaches, which we later show can be used to tune the photoelectrochemical properties of the TiO_2 NWs.

TEM and HRTEM were further carried out to confirm the morphologies of the pure TiO_2 and the TG core-shell structures. As shown in Fig. 2(d), the TEM image of a single nanowire in a representative TG10 sample reveals that GaO_xN_y covers the entire 1D TiO_2 NW, which is consistent with our previous reported for the ZnO-GaON systems[18]. Obviously, TiO_2 NW with a diameter of 22 nm was covered by an 8-nm thin shell of GaO_xN_y, in line with the SEM results in Fig. 2(c). The large and intimate interfacial contact between the core and the thin shell promotes the formation of a heterojunction between the TiO_2 and GaO_xN_y, which results in an enhanced transfer and separation of photogenerated charge carriers, thereby improving the photoelectrochemical activity as we will discuss later. The HRTEM image of TG10 in Fig. 2(e) reveals that two different fringes exist in the TG core-shell NWs. For the selected area in Figure 2(f), marked by the red frame, the lattice fringes with interplanar spacing of 0.32 nm are assigned to the d-spacing of the (112) crystallographic planes of rutile.[40] The TiO_2 growth direction of NWs was observed in the <001> direction, which is in accordance with XRD results indicating that the intensity of the (002) diffraction peak is stronger than that of the (101) peak. The HRTEM image of the GaO_xN_y shell,

as shown in Fig. 2(e), indicates poor crystallinity. In Fig. 2(g) and (h), two lattice spacing can be clearly identified with interplanar distances of 0.28 and 0.26 nm. These would be consistent with the interplanar distances of the (100) and (002) planes of GaN. However, no evidence for crystallization of Ga_2O_3 or GaON was found, which suggests that the GaO_xN_y shell may contain some possible mixture of crystalline GaN and amorphous Ga_2O_3 or GaON. Furthermore, the SAED (Selected area electron diffraction) pattern for TG10 (inset of Fig. 2(d)) can be indexed with the (001) and (210) planes of rutile TiO_2 and suggest that TG10 contains a GaO_xN_y shell. It is worth emphasizing that the content of crystalline GaN in GaON is very small, and the GaON modifiers are dominated by amorphous Ga_2O_3 and GaON (Fig. S3). Similar crystallization properties and phenomena have been observed during the growth of other complex metal oxides by ALD technology.[41]

The HAADF (High-angle annular dark field) image of a single TG core-shell NW in Fig. 2(i) demonstrates that the GaO_xN_y shell is brighter than the TiO_2 core. This arises from the mass contrast difference between the TiO_2 core and GaO_xN_y shell. Additionally, the line scanning results also demonstrate the distribution and configuration of Ga, Ti, O, and N, as shown in Fig. 2(j)-(m). Ti, O, and N are contained in the NW core, while Ga, O, and N are found in the shell. We note that the existence of elemental N in the core may be due to the Kirkendall effect.[42] These results indicate successful growth of a uniform GaO_xN_y shell on the TiO_2 NWs.

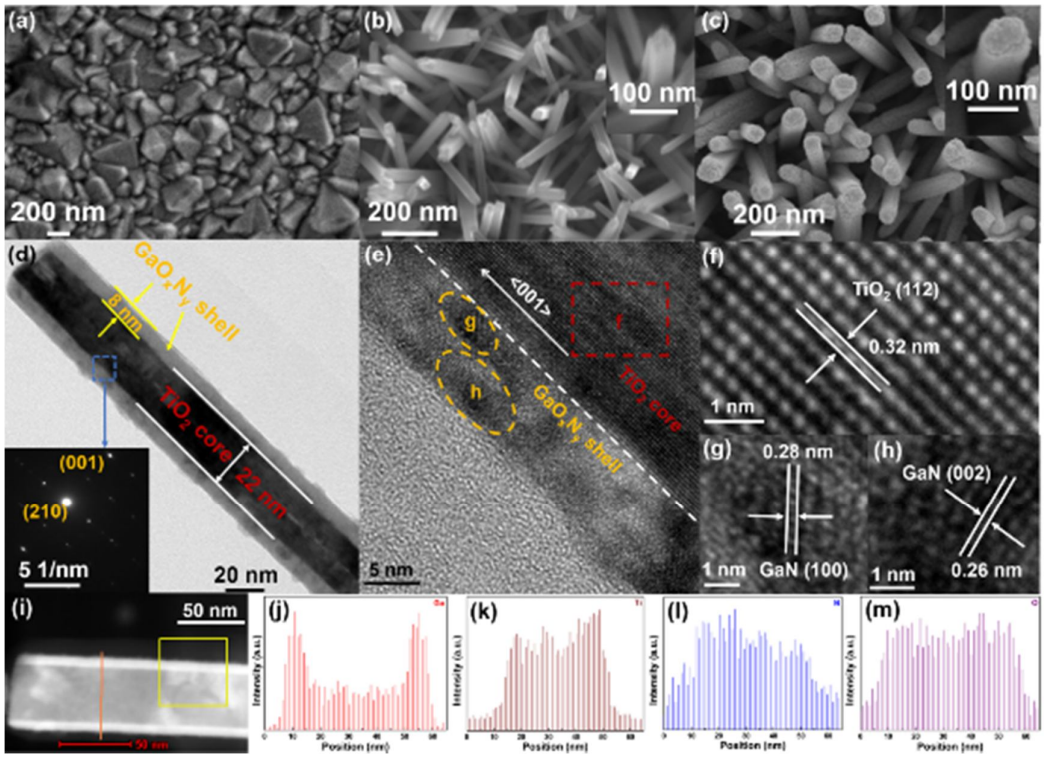

Fig.2 SEM images of (a) the FTO glass substrate, (b) pure TiO_2 NWs, and (c) TG10. Insets in (b) and (c) show the bottom view of TiO_2 and TG10. TEM image of (d) TG10, (e) HRTEM image of TG10 and (f) - (h) the designated f - h parts in Fig. 2(e). Inset in (d) shows the corresponding SAED pattern. (i) HAADF image of a single TG10 NW, and (j)-(m) line-scanning profiles of the elements Ga, Ti, N, and O across the TG10 nanowire (red line in the HAADF).

Given the limited penetration depth of the X-rays (*ca.* 10 nm) we use a representative thin TG5 sample for XPS analysis. The XPS spectra are shown in Fig. 3. The XPS survey spectra in Fig. S4 contain peaks for Ga 2p, O 1s, Ti 2p, N 1s, Ga 3s, Ga 3p, and Ga 2d, indicating the existence of N and Ga in the TG5 sample. This confirms the deposition of GaO_xN_y on the surface of TiO_2 NWs.

As shown in Fig. 3(a), the high-resolution spectrum of N 1s can be deconvoluted into two peaks. The peaks at 397.0 and 399.9 eV can be assigned to the Ga-N and Ga-O-N binding energies in GaN and GaON, respectively.[43] No other N chemical bonds, such as in NO_2 nitrite (404.5 eV) and NO_3 nitrate (406.8 eV) were observed, which reveal the high quality of the GaO_xN_y shells. It is important to note that doping N into metal oxides has always been a challenge, but this problem was resolved in our PE-ALD process. We estimate that 6.2% N is present from the XPS spectrum of TG5. Even with a relatively few PE-ALD cycles and a low NH_3 flow ratio (5 sccm), the GaO_xN_y shell shows significant atomic percentages of N. Having TG samples with a high N content is beneficial in enhancing the visible-light absorbance and photoelectrochemical performance as the N 2p states tend to shift the valance band edge to higher energy.[44]

In Fig. 3(b), the O 1s peaks consist of three components, corresponding to Ti-O (530.4 eV), Ga-O (530.7 eV), and Ga-O-N (532.4 eV),[45] suggesting the formation of a GaO_xN_y shell structure. The Ti 2p spectrum in Fig. 3(c) features two characteristic peaks at 457.9 and 463.6 eV, which correspond to $2p_{3/2}$ and $2p_{1/2}$, respectively. These peaks indicate that the presence of Ti^{4+} state in TG core-shell NWs, thus the oxidation state of Ti remains unchanged upon modification with GaO_xN_y by PE-ALD. Fig. 3(d) manifests Ga 2p spectrum, in which two peaks at 1144.5 and 1117.6 eV are assigned to the $2p_{1/2}$ and $2p_{3/2}$, respectively, and this is associated with Ga^{3+} cation oxidation state. The energy spacing between $2p_{1/2}$ and $2p_{3/2}$ was 26.9 eV, which is in agreement with

our previous reports for Ga 2p in GaZnO materials.[41]

Fig. 3(e) and (f) show high-resolution XPS spectra of Ga $2p_{3/2}$ and Ga 3d from the TG 5 sample. The peaks at 1118.1 and 1117.3 eV are, respectively, assigned to the Ga-O and Ga-N bonds, and the peaks at 22.4 and 20.1 eV, respectively, belong to the Ga-O and Ga-N bonds, further demonstrating the existence of Ga_2O_3 and GaN.[46]

Fig. S4 shows the XPS spectra for pure TiO_2. Upon comparing the XPS signals of O 1s and Ti 2p between TiO2 and TG5, we found that the disappearance of O-H bonds and slight red shift of Ti 2p. The disappearance of O-H bonds in TG5 is due to the epitaxial growth process of GaO_xN_y onto the external surface of the TiO_2. This can be proved by the small mismatch lattices between TiO_2 (0.32 nm of the (112) plane) and GaO_xN_y (0.28 nm 0.26 nm of (100) and (002) planes)[18], which provides the condition for the growth of crystalline GaO_xN_y even at the low ALD deposition temperature of 200 ℃, as shown in Fig.2(e)-(g). Furthermore, the TEM results also indicated that the coated GaON shell close contact with TiO_2 presented high crystallinity, while other layer was amorphous. The interface between crystal and amorphous in TG system benefits the effective electron hole separation and transmission and separation, enhancing the PEC performance [REFERENCES]. The slight red shift of Ti 2p may mainly attributed to the effect of hybridization of O 2p and N 2p states with Ga 3d orbitals[15], which promotes higher electron mobility to enhance the PEC performance, as we explained before.

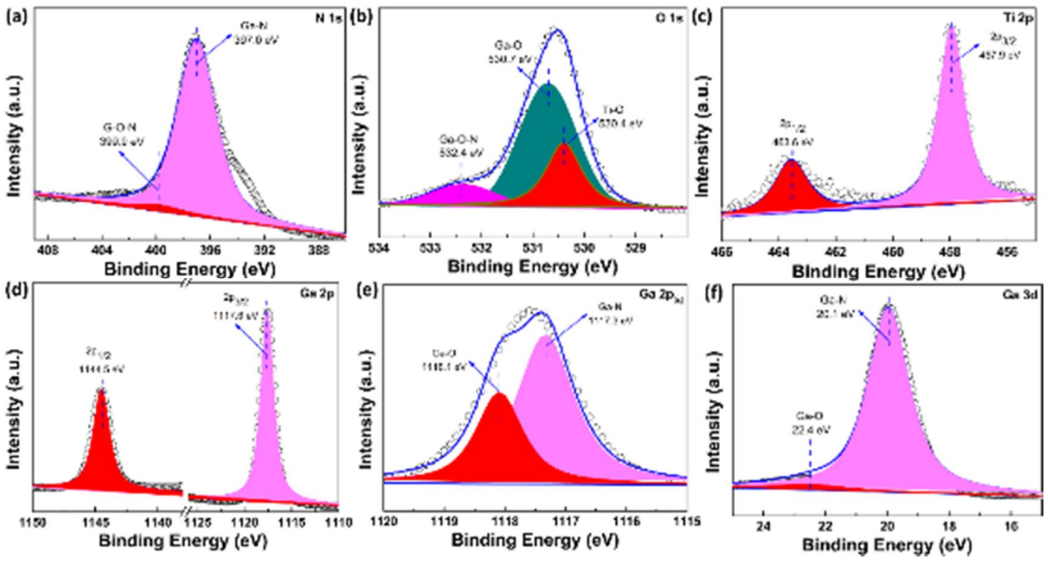

Fig.3 XPS spectra of the TG5 sample: (a) N 1s, (b) O 1s, (c) Ti 2p, (d) Ga 2p, (e) Ga $2p_{3/2}$, (f) Ga 3d.

The UV-Vis diffuse reflectance spectra (DRS) are presented in Fig. 4(a). For unmodified TiO_2 NWs, the significant absorption at wavelengths shorter than 366 nm in the UV is due to the intrinsic band gap absorption.[47,48] It is obvious that loading the GaO_xN_y onto the surface of TiO_2 NWs can broaden light absorption towards the visible light region. In addition, it appears that the absorption of light by the TG core-shell NWs is enhanced compared to unmodified TiO_2 NWs. The absorption edge of TG NWs also displays a red shift with an increase in the GaO_xN_y thickness. More importantly, the TG20 sample shows enhanced light absorption when compared to unmodified TiO_2 and other TG NWs, which reveals that the GaO_xN_y layer plays an important role in utilizing sunlight and that there is an optimum thickness of the GaO_xN_y shell. There is a small characteristic peak at 465 nm in the TG25 sample, which is likely due to a small amount of GaO_xN_y.[23] The energy band gap (E_g) is estimated from the conventional Tauc

equation:

$$(\alpha h\nu)^2 = A(h\nu - E_g) \quad (5)$$

where α denotes the absorption coefficient, *h* denotes Planck's constant, ν denotes the frequency of the incident photon, and A denotes a constant that depends on the electron or hole mobility.[49] The corresponding Kubelka-Munk-transformed reflectance spectra are exhibited in Figure 4(b). The calculated E_g from Fig. 4(b) is estimated to be 3.20 eV for pure TiO_2 NWs and 2.15 eV for TG25 NWs, indicating that the presence of GaO_xN_y strongly enhances light absorption in the visible region, which makes this heterostructured material suitable for visible light photoelectrochemical water splitting.

Fig. 4(c) shows that the direct gap transition energies of samples TG5 to TG25 were approximately 3.10, 3.02, 2.91, 2.58, and 2.15 eV. As implied in Figure 4(c), the nitride and oxide of gallium, GaN and Ga_2O_3 have band gap energies of 3.4 and 4.7 eV, respectively,[50] and can only absorb UV light. The variation in the TG band gap with changing GaO_xN_y thickness is therefore not driven by formation of bulk gallium oxides or nitrides, but is instead associated with the mixed oxygen and nitrogen compositions in GaO_xN_y, and the formation of the heterojunction with the TiO_2 NWs which leads to a reduction in the band gap over unmodified TiO_2. TG25 has the smallest band gap, probably due to the highest nitrogen and oxygen content, which would cause a high degree of O_{2p} with N_{2p} orbital hybridization and shift the valence band maximum upwards via p-d repulsion as previously described.[25,51,52]

The TG25 sample shows a weaker light absorption than that of TG20 (>600 nm) in Fig.4a. It is proposed that the additional thick GaON shells (25 nm-GaO_xN_y) are now sufficiently thick that absorption is dominated by GaON rather than the GaON-TiO2, together with a decrease in the surface area of the 1D TiO_2 nanostructures which inhibits light absorption. As shown in Fig.4a, the GaO_xN_y film shows a decreasing absorption trend after the wavelength of 600 nm compared with TiO_2 and TG samples. Similarly, Khan et al.[4] also reported that the GaON shows a weaker light absorption than ZnO-GaON system with the increasing of the wavelength.

The carrier recombination, migration, capture, and separation of the photogenerated e^--h^+ pairs were studied by PL spectrometry. Fig. 4(d) shows the spectra of TiO_2 and TG NWs. Under an excitation wavelength of 320 nm, the typical broad emission band from 380 nm to 580 nm for rutile TiO_2 is observed. All samples show three characteristic peaks around 385, 420, and 466 nm, which can be attributed to the intrinsic emission of rutile TiO_2 and the band edge free excitons.[53] There are no new PL features present in the modified TG NWs. The intensity of the PL spectrum for TG NWs is much reduced compared to the pure TiO_2 NWs.[54,55] In addition, as the thickness of the GaO_xN_y layer increases, the emission intensity decreases down to the first minimum in sample TG20, and then increases in sample TG25. The lower PL intensity of TG20 implies that the modification with GaO_xN_y impedes the recombination of e^- and h^+, which is clearly beneficial to the photocatalytic performance.[56] Based on the analysis above, we speculate that the TG20 should exhibit the best

photoelectrochemical performance of our samples, which is discussed below.

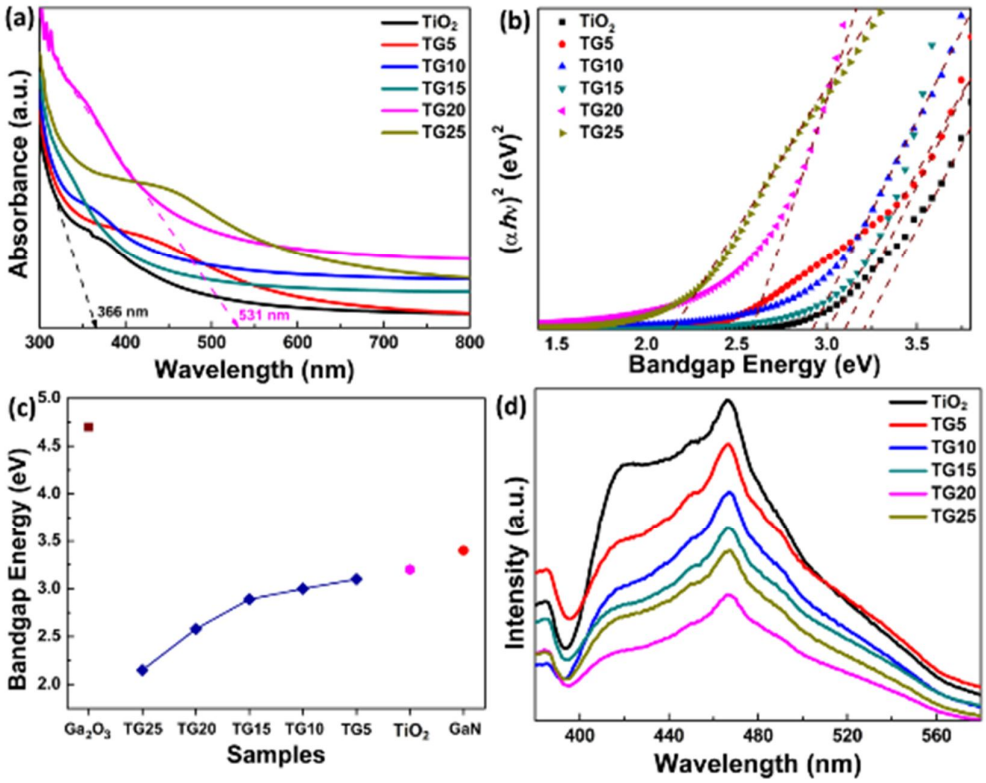

Fig.4 (a) Diffuse reflectance spectra of the TiO_2 NWs and different TG NWs, (b) plots of $(\alpha h\nu)^2$ versus bandgap energy for direct gap transition of the TiO_2 NWs and different TG NWs, (c) band gap energy of the TiO_2 NWs and different TG NWs. The band gap energies of Ga_2O_3 and GaN are also provide in panel (c). (d) PL spectra of the TiO_2 NWs and different TG NWs.

Photoelectrochemical performance

The PEC performance results were collected by systematic photocurrent response tests as shown in Fig. 5. The dark current densities of all samples were first tested and are presented in Fig. 5(a), which clearly indicate no significant dark current, confirming

that the photocurrent density mainly comes from photocatalytic water reaction. Fig. 5(b) displays the current density-potential (*J-V*) curves of TG NWs under illumination. The current density increases with the increase of voltage for all samples. Compared with the pure TiO_2 NWs, the TG NWs all display higher current density. The current density for TiO_2, TG5, TG10, TG15, TG20, and TG25 were 0.08, 0.17, 0.36, 0.63, 1.10, 1.02 mA cm^{-2}, respectively at 1.23 V *vs* RHE. As the shell thickness of the GaO_xN_y modifier increases, the current density first shows an increase and then a decrease for the thickest GaO_xN_y shell. Among all TG NWs samples, TG20 shows the highest current density of about 1.10 mA cm^{-2} at 1.23 V *vs.* RHE (i.e. 0.63 V vs Ag/AgCl), which is almost 14 times than that of our pure TiO_2 NWs (0.08 mA cm^{-2}). These results indicate that the fabrication of TG core-shell structure strongly enhances the photoactivity of TiO_2 NWs and this can be controlled by the thickness of the GaO_xN_y shell deposited by ALD. The significant enhancement in current density is due to the advantageous features of TG core-shell heterostructure NWs. This structure results in efficient charge separation. In addition, other than the raised current density, the onset potentials of these TG NWs exhibited a remarkable and negative shift with respect to pure TiO_2 NWs, which indicates that more e^- are liberated and accumulated in the TG NWs. This can be attributed to favorable effect of GaO_xN_y, which decrease the kinetic energy barrier of charge transfer among the interface of GaO_xN_y and TiO_2.[57]

Fig. 5(c) displays the current-time (*I-t*) curves of pure TiO_2 and different TG NWs. The transient photocurrent responses were conducted with the interval 15 s light

ON/OFF cycle at 1.23 V (*vs* RHE). The enhanced photocurrent density changes in the order of TG20 > TG25 > TG15 > TG10 > TG5 > TiO_2, indicating that the TG20 is the optimum shell thickness to facilitate the separation of photogenerated charge carriers, which is in accordance with the previous *J-V* measurement results. TG samples show good photoswitching properties with a rapid response speed, which is stable and reproducible. Obviously, the TG20 showed the maximum increase to 1.06 mA cm^{-2} in several cycles, which is almost 18 times higher than pure TiO_2 (0.06 mA cm^{-2}). The light current-dark current ratio of TG20 is 1.9×10^3 and the photocurrent decays to stable state in less than 1 s. Moreover, as shown in Fig. 5(d), the TG20 sample shows almost no changes in photocurrent density at fixed current even with 10 h of continuous light irradiation. The SEM images of TG20 before and after PEC measurement in Fig. S5 shows no noticeable degradation of the TG20 NWs. These results further demonstrate that TG20 has excellent structural stability and photoelectric durability. Electrochemical impedance spectroscopy (EIS) was also applied to analyse the interfacial charge transfer and separation efficiency between the electrolyte and sample. As shown in Fig. 5(e), the semicircle radius on the plot of TG samples are smaller than that of TiO_2, revealing that the formation of core-shell structure between TiO_2 and GaO_xN_y enhances charge carrier separation and transport. Among these TG samples, TG20 possesses a more depressed semicircle, which demonstrates a faster charge carrier transfer rate and smaller resistance and compared to TiO_2 NWs. Furthermore, the Nyquist plots can be fitted to the equivalent Randle circuit as shown in the inset of Fig. 5(e) for studying the impedance. In the equivalent Randle circuit, there are three

main electronic components: the charge transfer resistance (R_{ct}), the series resistance (R_s), and constant phase element (CPE).[58] The R_{ct} reflects the charge transfer resistance at TG NWs electrode and electrolyte interface and within TiO_2 NWs. This corresponds to a high frequency semicircle, which is equal to the second large semicircle in Fig. 5(e). In general, a smaller R_{ct} means a faster reaction rate. Table S1 summarizes the values of R_{ct} according to the electrochemical fit and simulation. Compared to other TG systems and TiO_2 NWs, the TG20 shows the lowest R_{ct} value, which confirms the improved separation efficiency of photogenerated carriers and the faster charge transfer at the interface of TG20 NWs and electrolyte.[59]

In order to illuminate the role of the GaO_xN_y shell in improved PEC performance, we also measured the incident photon to current conversion efficiency (IPCE) to characterize the wavelength dependent photoresponse. As displayed in Fig. 5(f), the IPCE spectra was obtained for pure TiO_2 NWs as well as for best photoresponsive TG20 NWs. The IPCE data collected from TG20 NWs displayed an enhancement over the entire wavelength range compared to pure TiO_2 NWs. Further, the maximum IPCE value of 30.44% for TiO_2 NWs at the wavelength of 380 nm is significantly increased to a value of 92.08% at 380 nm for TG20. Although the IPCE is low in the longer wavelength, 400-460 nm, we can still see the enhanced IPCE values for TG20 compared to TiO_2 NWs. These are consistent with the results of the absorption spectrum and PEC measurements. The increased IPCE values with increasing the wavelength suggests that GaO_xN_y shell narrows the effective bandgap of TiO_2 NWs, which

improves the light collection and conversion efficiency particularly in the visible region. These results show that the unique TG core-shell NWs with appropriate shell thickness can enhance the PEC performance of TiO_2 NWs.

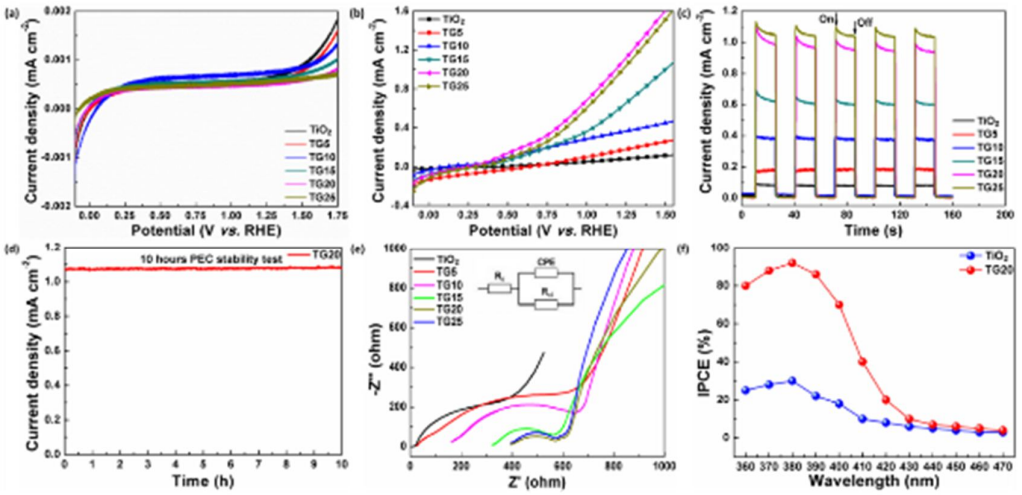

Fig.5 (a) LSV spectra in dark and (b) light, (c) I-t curves, (d) PEC stability studies of TG20 for 10 h, (e) EIS plots, (f) IPCE spectra for TiO_2 and TG20 NWs. The inset of (e) shows the equivalent fitting circuit.

In our work, the enhancement percentage (EP) for PEC performance of TG20 to TiO2 was calculated by the following formula and shown in Fig. A7.

(1)

Compared with the bare TiO2, the 20 nm-GaOxNy modified TiO2 (TG20) shows enhanced PEC performance in the wavelength of 360-470 nm, especially in the wavelength of 360-420 nm. A small amount of GaOxNy modification cannot completely replace the function of TiO2, but only enhance the PEC performance of

specific wavelength. In fact, a similar conclusion was drawn in our recent ZnO-GaON system2. Therefore, it can be concluded that the enhancement of the PEC performance of the TG system compared to the TiO2 NWs is significant in the UV region and the enhancement is smaller under visible light irradiation.

Table 1 presents a comparison of the PEC performance of various TiO_2 and GaO_xN_y based photocatalysts. The single TiO_2 and Ga-based materials have rather low photocurrent density values, such as the 0.013 mA cm^{-1} for TiO_2 NWs,[60] the 0.28 mA cm^{-1} for GaON nanosheets,[24] and 0.20 mA cm^{-1} for flat porous GaN.[62] Similarly, the optimized GaO_xN_y based composites still show low photocurrent density. For example, the photocurrent densities for a $BiVO_4/GaO_xN_{1-x}$ composite[63] and for $(GaN)_{1-x}(ZnO)_x$[64] are 0.37 and 0.03 mA cm^{-1}. In contrast, the TG20 NWs synthesized by a combination of hydrothermal synthesis and PE-ALD deposition in this work already display a large photocurrent density of 1.10 mA cm^{-1} at 1.23 V *vs* RHE in 0.5 M $NaSO_4$ solution.

Table 1 Comparison of the PEC performance of the TiO_2 and GaO_xN_y based photocatalysts.

Materials	**Methods**	**Electrolytes**	**Applied voltage (V)**	**Photocurrent density ($mA\ cm^{-2}$)**	**Reference**
TiO_2 NWs	Hydrothermal Method	0.5 M Na_2SO_4	1.23 V vs Ag/AgCl	0.013	60

GaON Nanosheets	Hydrothermal Method	0.5 M Na_2SO_4	0.60 V vs SCE	0.28	24
β-Ga_2O_3 Nanoparticles	RF Sputtering	1 M NaCl	0.2 V vs Ag/AgCl	0.002	61
Flat porous GaN	Thermal Ammonia Treatment	0.5 M Na_2SO_4	1.23 V vs Ag/AgCl	0.20	62
$BiVO_4/GaO_xN_{1-x}$	Sol-Gel Spin Coating	0.5 M K_3PO_4	1.23 V vs Ag/AgCl	0.37	63
$(GaN)_{1-x}(ZnO)_x$	Solution Method	0.5 M $NaSO_4$	1.23 V vs RHE	0.03	64
GaON/TiO_2 NWs	**Hydrothermal Method & ALD**	**0.5 M $NaSO_4$**	**1.23 V vs RHE**	**1.10**	**This work**

Origin of enhanced performance

The origin of enhanced PEC performance of the TG NWs is now discussed in detail. Firstly, as shown in Fig. 4(a), in the diffuse reflectance spectra of the TiO_2 NWs and our range of TG NWs we see that compared with pure TiO_2 NWs, the TG NWs show a clear red shift of the absorption edge. This observed enhancement in visible light absorption is attributed to the strong effect of the GaO_xN_y on the position of the valence band edge as discussed in the DFT results below. TG20 shows the strongest absorption ranging from 400 to 600 nm. This can be due to the fact that the TG core-shell NWs provides a longer light transport path,[65] thus enhancing the PEC performance. Secondly, in Fig. 6(a), we show results based on the finite difference time domain (FDTD) method, in which the electric-field distribution for single TiO_2, TG10, and TG20 NWs were simulated at an excitation wavelength of 420 nm. The corresponding simulation models are shown in detali in Fig. S6. To simplify the simulation model, the

protrusion of the top of the nanowires is ignored, and the geometric dimension parameters are obtained according to the SEM and TEM results. The electric-field intensity in TG10 and TG20 are greatly enhanced compared with pure TiO_2 NWs, and this indicates much higher possibilities for excitation of charge carriers in TG samples. In addition, the GaO_xN_y shell thickness of 20 nm is the most favorable for light reflection and interference, and this can promote the diffusion and transfer of holes in the TiO_2 core and GaO_xN_y shell.[66] Thus, in the present work, the enhancement of light absorption in the TiO_2 core and GaO_xN_y shell can more effectively promote the generation and separation of photoexcited e^--h^+ pairs, which drives the enhanced PEC performance of the core-shell NW structures.

Fig. 6(b) shows the VB XPS spectra of TiO_2 and TG5. From the spectra, the valence band energy (E_v) of TiO_2 and TG5 are calculated to be 2.26 and 1.22 eV, respectively. From Fig. 4(b), the band gap of TiO_2 and TG5 are estimated to be 3.20 and 3.10 eV, respectively. Thus, the conduction band energies (E_c) are calculated to be - 0.94 and - 1.88 for TiO_2 and TG5 versus normal hydrogen electrode (NHE) from E_g-E_V. Notably, Compared with TiO_2, TG5 has a higher CB minimum, as shown in Fig. 6(c), which can promote the electrons migration to the conduction band, thus enhancing reduction capacity and driving the reduction reaction more effectively. Iqbal et al.,[24] reported that the E_{CB} and E_{VB} of GaON are more negative than those of TiO_2, which suggests that core-shell NW-TG structure can promote the transfer of electrons and holes. In terms of band structure, the TiO_2 core and GaO_xN_y shell structure achieves a

favourable alignment. Moreover, the VB of TG5 is below the oxidation level for H_2O to O_2 while the CB is above the reduction level for H_2O to H_2.[47] Thirdly, based on the analysis above, to explain the improved PEC performance and stability of TG core-shell NWs, the charge transfer mechanism of photogenerated carriers is schematically shown in Fig. 6(d). The TG core-shell NWs show enhanced light harvesting capacity in both UV and visible region. It is well known that photogenerated carriers can be transferred from one semiconductor to another with suitable band alignment matching. Under light illumination, photo excitation will occur into the CB of the TiO_2 core from the GaO_xN_y shell, leaving holes in the VB.[67] The type-II band alignment, as shown in Fig. 6(c), promotes the transfer of photogenerated electrons from the CB of GaO_xN_y to the CB of TiO_2. Then the electrons transfer from TiO_2 to FTO by the back contact, finally to the Pt counter electrode and can reduce H^+ to H_2. On the other hand, the photogenerated holes migrate from TiO_2 into the higher lying valence band states of GaO_xN_y and can oxidise water molecules to generate O_2. The recombination ratios of electrons and holes for example of TG20 is strongly decreased, as indicated by the PL results in Fig. 4(d). In addition, the Nyquist plots (Fig. 5(e)) further supported this result, indicating a more effective separation of electron holes, which enhances the PEC performance.

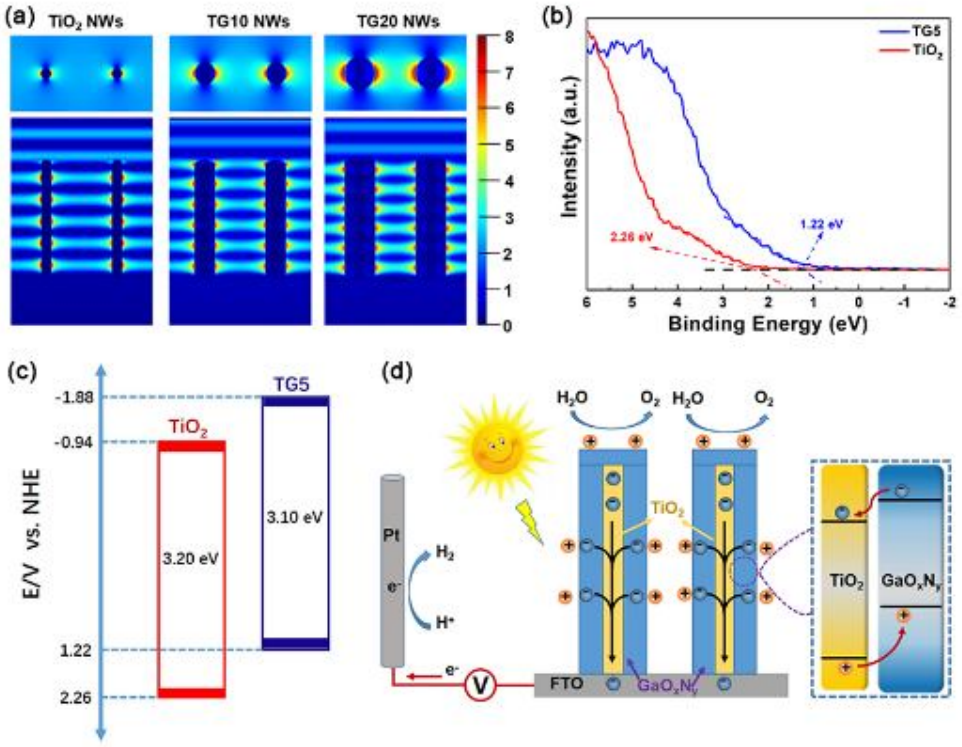

Fig.6 (a) Spatial distribution of electric-field for TiO_2, TG10, and TG20 core-shell NWs in a longitudinal view with ultraviolet (420 nm) incidence, (b) valence-band XPS spectra, (c) band structure diagram of the TG5 and TiO_2, and (d) schematic diagram of the PEC reaction mechanism of TG core-shell NWs.

We now discuss our results on DFT studies of a model GaO_xN_y-modified rutile (110) system. Firstly, we consider the formation of oxygen vacancies. As discussed in the experimental work earlier, this can be a key factor in the reactivity of these heterostructured core-shell materials. To investigate this aspect, we remove oxygen atoms from GaO_xN_y and compute the oxygen vacancy formation energy in heterostructures with composition $Ga_6O_5N_4$-TiO_2 and $Ga_6O_6N_3$ as described in Section 4. Fig. 7(a) and (b) display the atomic structure of two reduced GaO_xN_y-rutile (110)

structures with compositions $Ga_6O_4N_4$ and $Ga_6O_5N_3$. The corresponding computed oxygen vacancy formation energies are - 0.5 eV and - 0.3 eV, which means that these structures are more stable when off - stoichiometric due to loss of oxygen, which is consistent with the results from the experimental analysis.

Fig. 7(c) displays the projected electron density of states (PEDOS) plots for the example of the GaO_4N_4-modified rutile (110) model system. The PEDOS is projected onto the Ti 3d, Ga 4s and 4p and O 2p/N 2p states and the bottom row shows the PEDOS around the valence and conduction band edges. For this and all examined GaON-modified rutile (110) structures we find new states in the original rutile valance to conduction band energy gap, which arise from the modification of rutile (110) with the GaO_xN_y clusters. The highest occupied states lie at higher energy than the TiO_2 valance band edge, while the bottom of the conduction band is composed of Ti 3d states from the surface. The character of the highest occupied electronic states and the lowest conduction band states from the DFT+U analysis is consistent with the experimental results described above. While the quantitative changes in the energy gap cannot be fully captured by the DFT+U approach due to the inherent band gap underestimation, the introduction of new states in the energy gap arising from the GaO_xN_y modification and a red shift in light absorption to longer wavelength is consistent with the experimental findings, confirming that this interfacial system can enhance visible light absorption. The presence of GaO_xN_y - derived electronic states in the TiO_2 band gap persists upon reduction so the light absorption properties will not be affected by the

stoichiometry.

Upon reduction, the two electrons released after loss of oxygen localize onto two Ti atoms of the TiO_2 surface, one of which lies directly under the GaO_xN_y modifier and the second electron localizes on a Ti site in the subsurface layer. This reduction of Tis confirmed by computed Bader charges of 1.7 and 1.8 electrons for these Ti (giving net charges of 2.3 and 2.2 electrons) and computed spin magnetisations of 0.85 μ_B, both of which are consistent with a Ti^{3+} oxidation state.

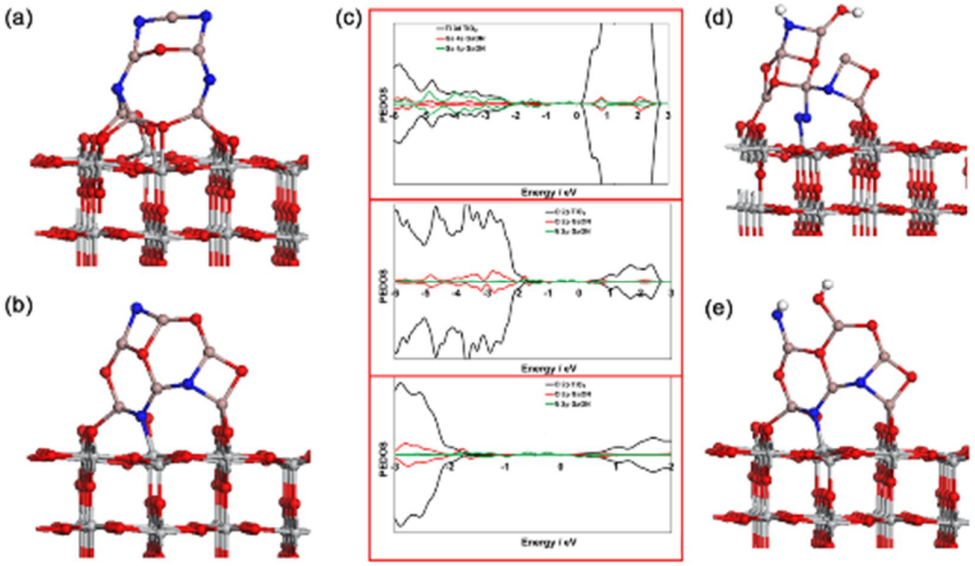

Fig.7 (a) Atomic structure of a reduced $Ga_6O_4N_4$-rutile structure formed by removing oxygen from $Ga_6O_5N_4$-rutile (110), (b) Atomic structure of a reduced $Ga_6O_5N_3$-rutile structure formed by removing oxygen from $Ga_6O_8N_3$-rutile (110), (c) Projected electronic density of states for the structure in (a), with the Fermi energy set to 0 eV. (d) Atomic structure of water adsorbed at reduced $Ga_6O_4N_4$-rutile, (e) Atomic structure of water adsorbed at reduced $Ga_6O_5N_3$-rutile. The grey spheres represent Ti, red spheres

O, blue spheres N, salmon spheres Ga and white spheres H.

We now consider the adsorption of water at the TiO_2@$Ga_6O_4N_4$ and the TiO_2@$Ga_6O_5N_3$ structures, in which both have a reducing oxygen vacancy. The relaxed water adsorption structures are shown in Fig. 7(d) and (e). The initial adsorption mode of water is molecular and upon relaxation, the water molecule always dissociates to form a hydroxyl (OH from water) and an NH species. The computed dissociative adsorption energies of a water molecule are - 0.72 eV and - 1.07 eV, suggesting a strong interaction between water and the TG system. However, the magnitude of the adsorption energy of water is moderate which suggests that the dissociated water is not merely forming a strongly bound hydroxyl species but can instead be active in the water oxidation process to produce oxygen. The direct dissociation of water is promoted by the presence of the reduced cations after forming the oxygen vacancy, which has been discussed in other studies.[68,69]

4. Conclusions

In summary, the TiO_2@GaO_xN_y core-shell nanowires photocathode for solar water splitting have been fabricated through hydrothermal and ALD technology and studied photoelectrochemically. By precise controlling the thickness of GaO_xN_y shell from ALD, when the thickness of GaO_xN_y is 20 nm, the TG20 core-shell NWs shows a significant photocurrent density of 1.10 mA cm^{-2} at 1.23 V *vs.* RHE under AM 1.5 G irradiation, which is 14 times larger than that of TiO_2 NWs. The TG20 also exhibits good stability. The enhanced PEC performance are attributed to the extended visible

light absorption, proper band alignment in TG core-shell system, making the effectively generation and transformation of photoexcited electrons and holes, and avoiding the interfacial recombination. In addition, the results of FDTD simulations and DFT calculations also suggest that the significant enhanced PEC performance in TG system for the existence of GaO_xN_y cluster, which is in accordance with the results of our experiment. It is anticipated that this approach may have considerable effect on the development of highly efficient and stable GaO_xN_y and TiO_2 based nanoarchitectures for environment sustainability.

Acknowledgments

This work is supported by the National Key R&D Program of China (No.2016YFE0110700), National Natural Science Foundation of China (No. U1632121, 11804055, 51861135105 and 61874034), Natural Science Foundation of Shanghai (No. 18ZR1405000), and China Postdoctoral Science Foundation (No. 2018M631997). This work is also supported by the Fudan University Exchange Program Scholarship for Doctoral Students. The work at Tyndall Institute is supported by Science Foundation Ireland through the SFI-NSF China Partnership Program, Grant Number SFI 17/NSFC/5279 NITRALD. We acknowledge access to computing resources at Tyndall supported by SFI and access to the SFI/DES/HEA funded Irish Center for High End Computing. The authors would also like to thank Prof. Xiaoxiang Xu of Tongji University and Prof. Yifang Chen of Fudan University, for the tests of photoelectrochemical performance and scanning electron microscopy.

Notes and references

1 G. Yilmaz, C.F. Tan, Y.F. Lim and G.W. Ho, *Adv. Energy Mater.*, 2019, **9**, 1802983.

2 J. Wang, C. Xue, W.Q. Yao, J. Liu, X.X. Gao, R.L. Zong, Z. Yang, W.J. Jin and D.P. Tao, *Appl. Catal. B - Environ.*, 2019, **250**, 369-381.

3 X.C. Huai, L. Girardi, R. Lu, S. Gao, Y. Zhao, Y.H. Ling, G.A. Rizzi, G. Granozzi and Z.J. Zhang, *Nano Energy*, 2019, **65**, 104020.

4 H. Li, P. Wen, D.S. Itanze, M.W. Kim, S. Adhikari, C. Lu, L. Jiang, Y.J. Qiu and S.M. Geyer, *Adv. Mater.*, 2019, **31**, 1900813.

5 S.C. Wang, G. Liu and L.Z. Wang, *Chem. Rev.*, 2019, **119**, 5192-5247.

6 A. Fujishima and K. Honda, *Nature*, 1972, **238**, 37-38.

7 N. Wei, Y. Liu, M. Feng, Z.X. Li, S.G. Chen, Y.B. Zheng and D.A. Wang, *Appl. Catal. B - Environ.*, 2019, **244**, 519-528.

8 L. Kang, L.P. Han, J.B. He, H.R. Li, T.T. Yan, G.R. Chen, J.P. Zhang, L.Y. Shi and D.S. Zhang, *Environ. Sci. Technol.*, 2019, **53**, 938-945.

9 Y. Liu, J. Xu, H.R. Li, S.X. Cai,H. Hu, C. Fang, L.Y. Shi and D.S. Zhang, *J. Mater. Chem. A*, 2015, **3**, 11543-11553.

10 K.W. Zha, C. Feng, L.P. Han, H.R. Li, T.T. Yan, S.C. Kuboon, L.Y. Shi and D.S. Zhang, *Chem. Eng. J.*, 2020,**381,** 122764.

11 J. Deng, Y.D. Su, D. Liu, P.D. Yang, B. Liu and C. Liu, *Chem. Rev.*, 2019, **119**, 9221-9259.

12 W. Yang and J. Moon, *ChemSusChem*, 2019, **12**, 1889-1899.

13 H.P. Zhou, M.L. Feng, K. Song, B. Liao, Y.C. Wang, R.C. Liu, X.N. Gong, D.K. Zhang, L.F. Cao and S.J. Chen, *Nanoscale*, 2019, **11**, 22871.

14 K. Wang, D.W. Huang, L. Yu, K. Feng, L.T. Li, T. Harada, S. Ikeda and F. Jiang, *ACS Catal.*, 2019, **9**, 3090-3097.

15 N. Arai, N. Saito, H. Nishiyama, K. Domen, H. Kobayashi and Y. Inoue, *Catal. Today*, 2007, **129**, 407-413.

16 H. Bae, H. Kim, J.W. Ju, D.W. Jeon, S.W. Ryu, Y. Moon and J.S. Ha, *J. Electrochem. Soc.*, 2019, **166**, H103-H107.

17 M.A. Hassan, J.H. Kang, M.A. Johar, J.S. Ha and S.W. Ryu, *Acta Mater.*, 2018, **146**, 171-175.

18 H.P. Ma, J.H. Yang, J.J. Tao, K.P. Yuan, P.H. Cheng, W. Huang, J.C. Wang, Q.X. Guo, H.L. Lu and D.W. Zhang, *Nano Energy*, 2019, **66**, 104089.

19 S.S. Patil, M.A. Johar, M.A. Hassan, D.R. Patil and S.W. Ryu, *Appl. Catal. B - Environ.*, 2018, **237**, 791-801.

20 H.Y. Chen, L.P. Wang, J.M. Bai, J.C. Hanson, J.B. Warren, J.T. Muckerman, E. Fujita and J.A. Rodriguez, *J. Phys. Chem. C*, 2010, **114**, 1809-1814.

21 I. Khan, A. Qurashi, G. Berdiyorov, N. Iqbal, K. Fuji and Z.H. Yamani, *Nano Energy*, 2018, **44**, 23-33.

22 S. Yu, B. Liu, Q. Wang, Y. Gao, Y. Shi, X. Feng, X. An, L. Liu and J. Zhang, *ACS Appl. Mater. Interfaces*, 2014, **6**, 10283-10295.

23 M. Zhong, Y. Ma, P. Oleynikov, K. Domen and J.J. Delaunay, *Energy Environ. Sci.*, 2014, **7**, 1693-1699.

24 N. Iqbal, I. Khan, Z.H. Yamani and A. Qurashi, *Sci. Rep.*, 2016, **6**, 32319.

25 C.C. Hu and H. Teng, *J. Phys. Chem. C*, 2010, **114**, 20100-20106.

26 J.J. Tao, H.L. Lu, Y. Gu, H.P. Ma, X. Li, J.X. Chen, W.J. Liu, H. Zhang and J.J. Feng, *Appl. Surf. Sci.*, 2019, **476**, 733-740.

27 S.C. Han, Y.C. Pu, L.X. Zheng, L.F. Hu, J.Z. Zhang and X.S. Fang, *J. Mater. Chem. A*, 2016, **4**, 1078-1086.

28 G. Kresse and J. Hafner, *Phys. Rev. B*, 1994, **49**, 14251-14269.

29 G. Kresse and D. Joubert, P*hys. Rev. B*, 1999, **59**, 1758-1775.

30 J.P. Perdew, J.A. Chevary, S.H. Vosko, K.A. Jackson, M.R. Pederson, D.J. Singh and C. Fiolhais, *Phys. Rev. B*, 1992, **46**, 6671-6687.

31 M. Nolan, *Phys. Chem. Chem. Phys.*, 2011, **13**, 18194-18199.

32 S.L. Dudarev, G.A. Botton, S.Y. Savrasov, C.J. Humphreys and A.P. Sutton, *Phys. Rev. B*, 1998, **57**, 1505-1509.

33 G. Henkelman, A. Arnaldsson and H. Jónsson, *Comp. Mater. Sci.*, 2006, **36**, 354-360.

34 H.L Huang, X.L. Hou, J.R. Xiao, L. Zhao, Q.Y. Huang, H. Chen and Y.D. Li, *Catal. Today*, 2018, **330**, 189-194.

35 D. Machon, N.L. Bail, P. Hermet, T. Cornier, S. Daniele and S. Vignoli, *J. Phys. Chem. C*, 2019, **123**, 1948-1953.

36 L.K. Dhandole, M.A. Mahadik, S.G. Kim, H.S. Chung, Y.S. Seo, M. Cho, J.H. Ryu and J.S. Jang, *ACS Appl. Mater. Interfaces*, 2017, **9**, 23602-23613.

37 R. Gopal, A. Goyal, A. Saini, M. Nagar, N. Sharma, D.K. Gupta and V. Dhayal, *Ceram. Int.*, 2018, **44**, 19099-19105.

38 H.Y. Chen, H.L. Lu, J.X. Chen, F. Zhang, X.M. Ji, W.J. Liu, X.F. Yang and D.W. Zhang, *ACS Appl. Mater. Interfaces*, 2017, **9**, 38662-38669.

39 J.J. Tao, Z.Z. Gong, G. Yao, Y.L. Cheng, M. Zhang, J.G. Lv, S.W. Shi, G. He, X.S. Jiang, X.S. Chen and Z.Q. Sun, *J. Alloy. Compd.*, 2016, **688**, 605-612.

40 G.M. Wang, H.Y. Wang, Y.C. Ling, Y.C. Tang, X.Y. Yang, R.C. Fitzmorris, C.C. Wang, J.Z. Zhang and Y. Li, *Nano Lett.*, 2011, **11**, 3026-3033.

41 J.J. Tao, H.L. Lu, Y. Gu, H.P. Ma, X. Li, J.X. Chen, W.J. Liu, H. Zhang and J.J. Feng, *Appl. Surf. Sci.*, 2019, **476**, 733-740.

42 S.M. He, Y.Y. Meng, Q.L. Wu, J.L. Yang, S.C. Huang, X.H. Li, S.F. Tong, T. Asefa

and M.M. Wu, *Nanoscale*, 2018, **10**, 19367-19374.

43 K. Maeda, T. Takata, M. Hara, N. Saito, Y. Inoue, H. Kobayashi and K. Domen, *J. Am. Chem. Soc.*, 2005, **127**, 8286-8287.

44 F. Wang, X.X. He, L.M. Sun, J.Q. Chen, X.J. Wang, J.H. Xu and X.G. Han, *J. Mater. Chem. A*, 2018, **6**, 2091-2099.

45 W. Wei, Z. Qin, S. Fan, Z. Li, K. Shi, Q. Zhu and G. Zhang, *Nanoscale Res. Lett.*, 2012, **7**, 562.

46 M. Myers, F.L.M. Khir, M.A. Home, C. Mennell, J. Gillbanks, A. Tadich, M.V. Baker, B.D. Nener and G. Parish, *Appl. Surf. Sci.*, 2018, **435**, 23-30.

47 F. Guo, W.L. Shi, C. Zhu, H. Li and Z.H. Kang, *Appl. Catal. B - Environ.*, 2018, **226**, 412-420.

48 J.J. Li, S.C. Cai, E.Q. Yu, B. Weng, X. Chen, J. Chen, H.P. Jia and Y.J. Xu, *Appl. Catal. B - Environ.*, 2018, **233**, 260-271.

49 P. Li, H. Hu, J. Xu, H. Jing, H. Peng, J. Lu, C. Wu and S. Ai, *Appl. Catal. B - Environ.*, 2014, **147**, 912-919.

50 I.M. Høiaas, A.L. Mulyo, P.E. Vullum, D.C. Kim, L. Ahtapodov, B.O. Fimland, K. Kishino and H. Weman, *Nano Lett.*, 2019, **19**, 1649-1658.

51 K. Meada and K. Domen, *Chem. Mater.*, 2010, **22**, 612-623.

52 S. Shokhovets, L. Kirste, J.H. Leach, S. Krischok and M. Himmerlich, *J. Appl. Phy.*,

2017, **122**, 045706.

53 L. Li, J. Yan, T. Wang, Z. Zhao, J. Zhang, J. Gong and N. Guan, *Nat. Comm.*, 2015, **6**, 5881-5890.

54 M. Nolan, A. Lwaszuk, A.K. Lucid, J.J. Carey and M. Fronzi, *Adv. Mater.*, 2016, **28**, 5425-5446.

55 A. Iwaszuk, M. Nolan, Q.L. Jin, M. Fujishima and H. Tada, *J. Phys. Chem. C*, 2013, **117**, 2709-2718.

56 F. Tian, Y.P. Zhang, J. Zhang and C.X. Pan, *J. Phys. Chem. C*, 2012, **116**, 7515-7519.

57 S.X. Liu, L.X. Zheng, P.P. Yu, S.C. Han and X.S. Fang, *Adv. Funct. Mater.*, 2016, **26**, 3331-3339.

58 L.X. Zheng, W.W. Hu, X.W. Shu, H.J. Zheng and X.S. Fang, *Adv. Mater. Interfaces*, 2018, **5**, 1800515.

59 Y.J. Zhong, Z.S. Li, X. Zhao, T. Fang, H.T. Huang, Q.F. Qian, X.F. Chang, P. Wang, S.C. Yan, Z.T. Yu and Z.G. Zou, *Adv. Funct. Mater.*, 2016, **26**, 7156-7163.

60 Y.F. Wang, M. Zhang, H. Yu, Y. Zuo, J. Gao, G. He and Z.Q. Sun, *Appl. Catal. B - Environ.*, 2019, **252**, 174-186.

61 S.J. Chang, Y.L. Wu, W.Y. Weng, Y.H. Lin, W.K. Hsieh, J.K. Sheu and C.L. Hsu, *J. Electrochem. Soc.*, 2014, **161**, H508-H511.

62 H.J. Kim, J. Park, B.U. Ye, C.J. Yoo, J.L. Lee, S.W. Ryu, H. Lee, K.J. Choi and J.M.

Baik, *ACS Appl. Mater. Interfaces*, 2016, **8**, 18201-18207.

63 B.K. Kang, G.S. Han, J.H. Baek, D.G. Lee, Y.H. Song, S. Bin Kwon, I.S. Cho, H.S. Jung and D.H. Yoon, *Adv. Mater. Interfaces*, 2017, **4**, 1700323.

64 J. Li, B.D. Liu, A.M. Wu, B. Yang, W.J. Yang, F. Liu, X.L. Zhang, V. An and X. Jiang, *Inorg. Chem.*, 2018, **57**, 5240-5248.

65 K.P. Yuan, Q. Cao, H.L. Lu, M. Zhong, X.Z. Zheng, H.Y. Chen, T. Wang, J.J. Delaunay, W. Luo, L.W. Zhang, Y.Y. Wang, Y.H. Deng, S.J. Ding and D.W. Zhang, *J. Mater. Chem. A*, 2017, **5**, 14697-14706.

66 Z.M. Bai, X.Q. Yan, Y. Li, Z. Kang, S.Y. Cao and Y. Zhang, *Adv. Energy Mater.*, 2016, **6**, 1501459.

67 H. Ali, N. Ismail, A. Hegazy and M. Mekewi, *Electrochim. Acta*, 2014, **150**, 314-319.

68 S. Kenmoe, O. Lisovski, S. Piskunov, D. Bocharov, Y.F. Zhukovskii and E. Spohr, *J. Phys. Chem. B*, 2018, **122**, 5432-5440.

69 I.M. Nadeem, J.P.W. Treacy, S. Selcuk, X. Torrelles, H. Hussain, A. Wilson, D. C. Grinter, G. Cabailh, O. Bikondoa, C. Nicklin, A. Selloni, J. Zegenhagen, R. Lindsay and G. Thornton, *J. Phys. Chem. Lett.*, 2018, **9**, 3131-3136.